

Appraising the reliability of converted wavefield imaging: application to USArray imaging of the 410-km discontinuity

Xin Liu* and Gary L. Pavlis

Department of Geological Sciences, 1001 East 10th Street, Indiana University, Bloomington, IN 47405, USA. E-mail: xinliu@umail.iu.edu

Accepted 2012 November 26. Received 2012 November 8; in original form 2012 April 23

SUMMARY

We develop a generic method to appraise the reliability of wavefield imaging methods and use it to validate some novel observations on the 410-km discontinuity. The core concept of the error appraisal method is to produce a simulated data set that replicates the geometry of the real data. Here we implemented two simulation methods: (1) flat layer primary P to S conversions, and (2) a point source scattering model for P to S conversion data based on the Born approximation and ray theory propagators. We show how the approach can be extended for any simulation algorithm. We apply this new approach to appraise recent results using a 3-D, three-component P to S conversion imaging method applied to data collected by the USArray. Multiple metrics show that the amplitude of P to S converted energy scattered from the 410-km discontinuity varies by 18 dB with a systematically lower amplitude in an irregular band running from Idaho through northern Arizona. In addition, we observe strong lateral changes in the ratio of amplitudes recovered on the radial versus the transverse component. We compute point resolution functions and a checkerboard test to demonstrate we can reliably recover relative amplitudes with a lateral scale of the order of 200 km and a vertical scale of approximately 10 km. Irregular coverage locally distorts the amplitudes recovered in the checkerboard, but a 156 km scale checkerboard pattern is recovered. Flat layer simulations show we can recover relative amplitudes to within a range of 1 dB and the reconstructed transverse to radial amplitude is everywhere less than 0.1. A model with north–south oriented ridges with a 3° wavelength and 12.5 km amplitude shows of the order of ± 6 dB amplitude variations and small, but clear correlation of the transverse/radial amplitude ratio topography in the model. Finally, we model the 410-km discontinuity as a rough surface characterized by variations in amplitude and depth derived from the USArray data. The rough surface model recovers the scale of the observed amplitude variations, but does not explain the observed large variations in transverse component amplitudes imaged by the USArray data. The results indicate the 410-km discontinuity is definitely not a single interface separating isotropic media. We argue that it is likely better viewed as a rough surface with a structural fabric that creates anisotropic behaviour in some places.

Key words: Mantle processes; Theoretical seismology; Wave scattering and diffraction; North America.

1 INTRODUCTION

In the past decade scattered wave imaging methods have emerged as a common tool for imaging Earth structure in the lower crust and upper mantle. Two technical developments have made this possible. First, it was recognized in the 1970s that three-component, teleseismic P -wave data could be deconvolved to produce an approximation of the impulse response for P to S conversions (scattering) commonly called receiver functions (Vinnik 1977; Langston 1979). Second, in the late 1990s sufficiently dense portable array

data sets became available that full wavefield imaging methods became feasible. Dueker & Sheehan (1997) introduced the idea of common conversion point (CCP) stacking of receiver function data. CCP stacking is properly viewed as analogous to common midpoint (CMP) stacking in seismic reflection imaging (e.g. Pavlis 2003). The CMP analogue is a useful insight to understand why a series of seismic migration methods were quickly adapted to this variant of reflection processing. Many have used a form of simple ray backprojection (e.g. Dueker & Sheehan 1998; Niu *et al.* 2004; Eagar *et al.* 2010) where data are projected along ray paths and the final image is produced by a simple binned stack in a uniform grid defined on a 2-D section. Variants of Kirchhoff migration (Sheehan *et al.* 2000; Levander *et al.* 2005), finite difference

* Now at: University of Southern California, Los Angeles, CA, USA.

methods (Wilson *et al.* 2004), and Gaussian beam migration (Nowack *et al.* 2006) have been applied. Here we utilize results of a form of migration-inversion we call plane wave migration (Poppeliers & Pavlis 2003a; Pavlis 2011b).

Although scattered wave imaging methods have emerged as a core component of passive seismic array imaging, there have been limited attempts at appraising the reliability of the results. The only standard method that has been used is the bootstrap error estimation Efron (1979) first introduced for application to this problem by Dueker & Sheehan (1997). This is a purely statistical method that measures variations between data samples falling in a common CCP bin. It provides useful information, but does nothing to address a long string of limitations that are not really statistical in nature. Examples include: (1) scattering from unresolved small structure; (2) scattering from dipping interfaces not resolved with CCP bin spacing permitted by the data; (3) body wave to surface wave scattering; (4) multiples and (5) deconvolution noise. The first contribution of this paper is a general methodology for appraising scattered wavefield imaging. The basic idea is to construct a 3-D model of the subsurface and generate an exact simulation of every waveform that defines a data set. That data set is then run through the same imaging algorithm whose output we aim to appraise and the results are compared quantitatively. That method is generic and independent of the choice of how one simulates the real data. We also introduce a practical method for simulation of large data sets based on the Born approximation and the asymptotic theory of Beylkin & Burridge (1990). This method has a number of simplifying assumptions, but is less computationally demanding than what might be considered the ultimate simulation method: 3-D, elastic wave propagation models. We claim this method can be a useful component of the toolkit of colleagues doing this type of seismic imaging.

We demonstrate the utility of our error appraisal approach to evaluate new results from the USArray related to the 410-km discontinuity (hereafter referred to as the 410). The 410 is a global feature that marks the top of the region of the mantle commonly called the transition zone. It is defined in all modern, radially symmetric earth models by an upward step in *P*- and *S*-wave velocity around a depth of 410 km. A large literature exists of papers using seismic methods of various forms to investigate the 410 (for a fairly recent review see Helffrich 2000). A key reason why hundreds of papers have been written about the 410 and its sibling the 660-km discontinuity is that both are commonly linked to polymorphic phase changes in olivine which mineral physics data show have significant temperature dependence (e.g. Ringwood 1975). As a result a major theme in many papers on the topic is defining the depth to the top of the 410 and/or the 660-km discontinuity in order to illuminate variations in mantle temperature (Helffrich 2000).

Although hundreds of papers have been written about the 410, our results are unique. The primary reason for this claim is that no previous result on the 410 has the combined 3-D resolution and lateral coverage of this study. This is achieved with the combination of two components: (1) data from the largest seismic array ever deployed called the Earthscope Transportable Array (<http://www.earthscope.org>), which we will henceforth call simply the USArray and (2) the fully 3-D, vector wavefield imaging method applied to data from the USArray (the plane wave migration method of Pavlis 2011b). The comparable result is a recent paper by Cao & Levander (2010). However, their coverage and the volume of data they used is significantly smaller, the imaging methodology is less sophisticated, and they provide no error appraisal of any kind to evaluate their results. We use the error appraisal methods described

here to evaluate our results on imaging of the 410. Our results indicate the 410 is anything but a simple interface with gently varying topography. The high resolution, 3-D images produced by the plane wave migration method show that the 410 has wildly variable properties in space. Our error appraisal methods give a quantitative validation that these variations are real. In this paper, we touch only the surface of a potentially rich mother lode of new information the USArray may yield on the nature of the 410 using these new data and methods.

2 MODELLING THEORETICAL FRAMEWORK

2.1 Using forward models to appraise imaging results

The strategy we advocate here is necessary because of a fundamental difference between passive array data and seismic reflection data. It is not commonly appreciated that one of the secrets to the quality of modern seismic reflection imaging is the controlled, regular coverage of shot and receiver geometry. This means that unless there is extreme structure (e.g. salt) to drastically distort the incident wavefield the illumination within the study area (volume) is very regular. It also implies that although resolution is never perfect it is, by design, very uniform. This is not at all true of teleseismic *P* to *S* conversion imaging. The following all produce irregularities in the results whose impact we need assess to avoid erroneous interpretations: (1) irregular station coverage, (2) variable data quality (SNR) due to order of magnitude changes in source output amplitude and (3) the location of sources are not controlled but are at the mercy of where earthquakes occur on the planet during the data recording period. These factors produce irregular resolution characteristics as they do in seismic tomography, but with very different consequences. The error appraisal methods introduced here are aimed at appraising these irregular resolution characteristics.

The approach we advocate is effectively a form of hypothesis test. The approach can be thought of as four steps.

- (i) We construct a model, $\mathbf{m}(\mathbf{r})$, of the subsurface.
- (ii) We select a synthetic seismogram generator capable of simulation of any seismogram in the existing data set using \mathbf{m} . Use that generator to make a simulated copy of every seismogram in the data set. An element of this step worth noting but which we have not tested here is the source wavelet problem. That is, real teleseismic body waves have a common, unknown source wavelet that has to be deconvolved from the data. A complete simulation should apply variable source wavelet to each seismogram.
- (iii) Pass the simulation data through exactly the same processing sequence as the real data. This should include the deconvolution process to properly simulate potential deconvolution noise. We have not simulated the deconvolution process in this paper because the data we used [Earthscope Automated Receiver function Survey (EARS) (Crotwell & Owens 2005; Crotwell 2007)] made this intractable.
- (iv) Compare the simulated data image to \mathbf{m} and (optionally) the image produced from real data.

This approach is generic, but we now describe the specific implementations we have used in this paper to evaluate the nature of scattering from the 410.

2.2 Radially symmetric model

The first model we have used is the same as that described by Pavlis (2011b). We prescribe a layer boundary depth and assign a constant, angle independent amplitude for *P* to *S* conversions

from that horizon. Timing relations are computed from a specified radially symmetric earth model using the standard delay time equations for a spherical earth (e.g. Stein & Wysession 2003) and synthetic seismograms are computed by convolution with a specified wavelet. Neglecting multiples, geometric spreading corrections, and angle-dependent P to S conversion effects is, of course, unrealistic. Nonetheless, we show below that this provides a valuable first-order model for evaluating our results on the 410.

2.3 Point source model

The foundation of this method is a point source scattering model for elastic media based on the Born approximation. We use this as a basis for impulse, migration response estimates and to simulate scattering from a continuous surface by integration of point source solutions over a particular surface. It is ideal for the former, but may be less than optimal for the later. Continuous surface modelling may be more appropriately modelled by the Kirchhoff approximation as described by Bostock (2002), who provides a valuable comparison of results using the Born and Kirchhoff approximations. We also note that Shearer *et al.* (1999) used a comparable modelling method to that we developed to model SS precursors. SS precursors are underside reflections observed on transverse component seismograms. As a result they were able to use a simpler, isotropic scattering model. P to S conversions, which are the focus here, require a more complicated scattering model. The purpose of this section is to review the theoretical foundations and limiting approximations that are the basis of the method we developed.

The point source elastic scattering equations we use are found in the standard seismology textbook of (Aki & Richards 2002, chapter 13). That original work uses the representation theorem and the Born (single scattering) approximation to show that a perturbation of medium properties can be expressed as a set of body force equivalent forces that radiate as secondary sources. The theoretical understanding of this approach was extended by Wu & Aki (1985a,b) who recognized this method was valid only as an approximation of Rayleigh scattering. That is, the method we are using here is valid only when the length scale of the scattering body, $L \ll \lambda_{\min}$, where λ_{\min} is the wavelength of the highest frequency present in incident wavefield.

The point source (Green's function) scattering theory assumes a reference medium defined by a density field $\rho^0(\mathbf{x})$ and elastic properties described in the most general form by the compliance tensor field $c_{ijkl}^0(\mathbf{x})$. The actual medium is assumed to be related by small perturbations from the reference medium. We define the perturbation operator

$$\Delta L_{lp} = \Delta\rho \frac{\partial^2}{\partial t^2} \delta_{lp} - \frac{\partial}{\partial x_m} \Delta c_{lmpq} \frac{\partial}{\partial x_q}, \quad (1)$$

where $\Delta\rho = \rho - \rho^0$, $\Delta c_{lmpq} = c_{lmpq} - c_{lmpq}^0$.

The foundation of this paper is a later paper by Beylkin & Burridge (1990). Combining this with additional insights from Weglein *et al.* (2003) the theoretical foundation of this paper is the following general equation for the Born approximation in an elastic medium

$$\begin{aligned} \Delta G_{jk}(\mathbf{s}, 0; \mathbf{r}, t) &\approx \int \int \int_V (-\Delta L_{lp} \tilde{G}_{jp}) \star_\tau \hat{G}_{kl} dV \\ &= - \int \int \int_V \left[\Delta\rho \frac{\partial^2 \tilde{G}_{jl}}{\partial t^2} \star_\tau \hat{G}_{kl} \right. \\ &\quad \left. - \left(\Delta c_{lmpq} \frac{\partial \tilde{G}_{jp}}{\partial x_q} \right) \star_\tau \frac{\partial \hat{G}_{kl}}{\partial x_m} \right] dV, \end{aligned} \quad (2)$$

where $\Delta G_{jk} = \Delta G_{jk}(\mathbf{s}, 0; \mathbf{r}, t)$ is the scattered wave Green's function in the k -direction at receiver position \mathbf{r} and time t from a point force applied in the j -direction at the position \mathbf{s} and time 0. Here \tilde{G}_{jp} is the Green's function for the wavefield propagating from source to scattering point in the reference media and \hat{G}_{kl} denotes the Green's function for the wave propagating from scattering point to receiver in the reference media.

Although eq. (2) is an intermediate step for what we have actually implemented, we include it in this paper to emphasize two points. First, eq. (2) is a general result for the Born approximation in an elastic medium that provides physical insights not universally understood. The \tilde{G} terms are (Green's function) propagators that define wave propagation from a point source at position \mathbf{s} and with origin time 0 to the position of an inhomogeneity at position \mathbf{x} . The scattered wave amplitude is scaled by the strength of the perturbation at position \mathbf{x} defined by $\Delta\rho$ and Δc_{lmpq} . The scattered wave created by a mass inhomogeneity, $\Delta\rho$, radiates like a point force oriented in the direction of the particle motion of the incident wavefield at \mathbf{x} . Elastic property inhomogeneities radiate scattered waves like double couple (moment tensor sources). To clarify this we define

$$\Delta m_{ilm} = \Delta c_{lmpq} \frac{\partial \tilde{G}_{jp}}{\partial x_q} \quad (3)$$

as the equivalent moment rate tensor at the scattering point \mathbf{x} induced by the incident wavefield created by the source at position \mathbf{s} and time 0. The \hat{G} terms then describe radiation and propagation from the scattering point, \mathbf{x} to the receiver position \mathbf{r} . \hat{G}_{kl} is the impulse response (Green's function) for a point force applied in the l -direction at position \mathbf{x} and recorded in the k -direction at the receiver position \mathbf{r} . Similarly, $\frac{\partial \hat{G}_{jl}}{\partial x_q}$ is the propagator for the equivalent moment rate tensor at position \mathbf{x} and recorded at the receiver position \mathbf{r} . Both terms are 'illuminated' by the incident wave and the time base (the convolution, \star_τ symbol) is defined by the instantaneous acceleration ($\Delta\rho$ term) and instantaneous stress (equivalent moment tensor term) at the scattering point at \mathbf{x} . Note that the total scattered wavefield is the superposition of all first-order scattered waves within the volume V , which is the reason for the integral over V .

The second reason for including eq. (2) in this paper is that it is a more general result than the simplified version we describe next. The ideas of this paper could be extended using eq. (2) using either anisotropic elastic properties or more sophisticated propagators, so we give the more generic eq. (2) to help others move beyond what we give here.

Beylkin & Burridge (1990) derive the specialized forms of eq. (2) based on two additional simplified assumptions: (1) isotropic, elastic reference media and (2) the Green's functions are computed by ray theory. They derive the following term for P to S conversions

$$\Delta G_{jk} = \frac{\partial^2}{\partial t^2} \int \int \int_V f^{PS}(\theta^{PS}) \tilde{A}_j^P \hat{A}_{kl}^S \beta_l \delta(t - \phi^P - \phi^S) dV, \quad (4)$$

where f^{PS} is the scattering potential we define as

$$f^{PS}(\theta^{PS}) = -\rho_0 \left[\frac{\Delta\rho}{\rho_0} \sin \theta^{PS} + \frac{\Delta\mu}{\mu_0} \frac{c_S}{c_P} \sin 2\theta^{PS} \right] \quad (5)$$

with θ^{PS} defined as the angle between the incident P -wave ray path and the scattered S -wave ray path illustrated in Fig. 1(a). \tilde{A}_j^P and \hat{A}_{kl}^S are amplitude terms computed by ray theory while the ϕ terms defined traveltimes. Thus, the term $\delta(t - \phi^P - \phi^S)$ defines the scattered wave arrival time computed by ray theory for an impulse in

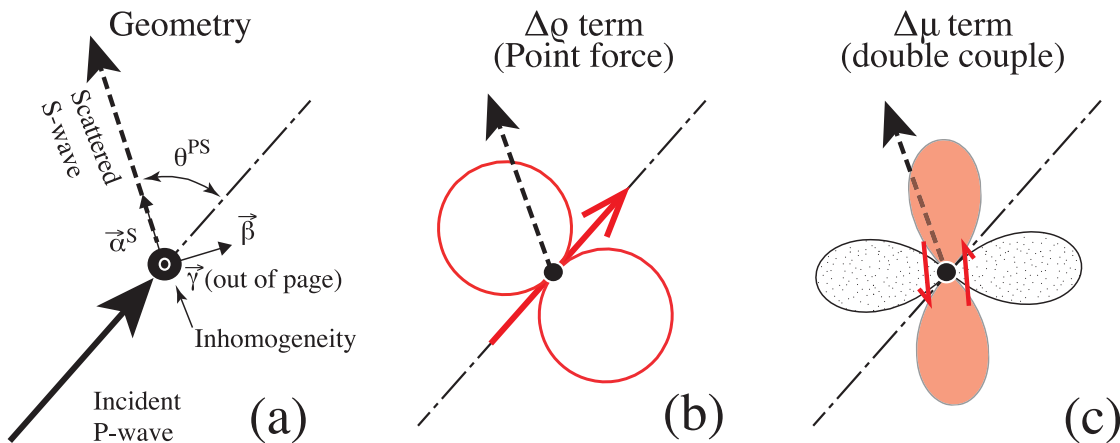


Figure 1. Point source scattering model geometry. Panel (a) illustrates coordinate system defined by Beylkin & Burridge (1990) and applied in this paper. The figure is in the plane formed by the incident P wave and scattered S -wave ray paths. Panel (b) shows the radiation pattern created by the density inhomogeneity term which acts as a point force along the direction of the incident P wave. Panel (c) shows the complementary radiation pattern for a shear modulus inhomogeneity, which radiates as a double couple source oriented as illustrated. It may be helpful to think of this as a consequence of a uniaxial stress field applied to the inhomogeneity by the incident P wave.

the j -direction at time 0 and position \mathbf{s} . $\tilde{\phi}^P$ is the P -wave traveltime from \mathbf{s} to \mathbf{x} and $\hat{\phi}^S$ is the S -wave traveltime from \mathbf{x} to \mathbf{r} .

Eq. (4) can be simplified for the teleseismic P -wave problem by assuming the entire volume is illuminated by a P wavefield with source–time function $S(t)$. This allows us to drop the vector dependence in the \tilde{A}^P term and write the following closed form for the P to S scattered wavefield at position \mathbf{r}

$$\begin{aligned} u_k(\mathbf{s}, \mathbf{r}, t) &= S \star_{\tau} \Delta G_k \\ &= \int \int \int_V f^{PS}(\theta^{PS}) \tilde{A}^P \hat{A}_{kl}^S \beta_l \frac{\partial^2 S}{\partial t^2}(t - \tilde{\phi}^P - \hat{\phi}^S) dV. \end{aligned} \quad (6)$$

In this theoretical framework we can compute the scalar amplitudes, \tilde{A}^P and $\|\hat{A}^S \beta\|$ using standard geometric spreading theory relations for a radially symmetric earth model (e.g. Stein & Wysession 2003, p. 187). The matrix \hat{A}_{kl}^S should be understood as a product of a scalar geometric spreading amplitude factor and a coordinate transformation. Liu (2011) shows the form of this transformation for a radially symmetric earth model which is a specialization of a comparable transformation described in Pavlis (2011b). The transformation matrix accounts for rotation of the converted S to maintain a polarization perpendicular to the ray path. The overall amplitude computed for a point scatter at \mathbf{x} recorded at \mathbf{r} is the product of three amplitude terms: (1) geometric spreading loss, A^P , for the incident P wave from \mathbf{s} to \mathbf{x} ; (2) the angle-dependent scattering term f^{PS} and (3) a geometric spreading term for the scattered S -wave, \hat{A}^S .

In our implementation of eq. (6) two variations are necessary. First, we are modelling data produced by conventional, single-station, receiver function estimated using the iterative deconvolution method of Ligorria & Ammon (1999) as implemented for the Earthscope Automated Receiver Survey (EARS) project. That single-station method autoscales the amplitude at every station so the actual output of the inverse wavelet and the recorded vertical signal has unit amplitude. For this reason we drop the \tilde{A}^P term assuming any such variations in the illuminating wave amplitude across the array is absorbed by the deconvolution process. Finally, the source–time function, S , in eq. (6) needs to be understood as the actual output of the deconvolution operator. This is actually somewhat ill defined for the iterative method, but we assume the actual output is the same as the Gaussian pulse convolved with the im-

pulse response computed in that method. Interestingly enough, if S is Gaussian the effective wavelet, $\frac{\partial^2 S}{\partial t^2}$, is the classic Ricker (Mexican Hat) wavelet commonly used in seismic reflection processing.

3 USARRAY IMAGING OF THE 410

We examined the 410 using the same image volume used by Pavlis *et al.* (2012), which is an update of the original plane wave migration result given by Pavlis (2011a). For details of this methodology the reader is referred to the original theoretical papers for the plane wave method Poppeiers & Pavlis (2003a,b) and the recent paper by Pavlis (2011b) which describes his implementation of the full 3-D algorithm. Furthermore, a novel element of the method described by Pavlis (2011b) is that it provides a vector estimate of scattering potential at each image point. It accomplishes this by computing a rotation matrix that is different for every three-component data sample. We would argue this is preferable to the more ambitious objective of using the data to estimate material properties of each point in the media as it requires no assumption about the nature of the target and is less demanding on the data. This can be viewed as analogous to seismic reflection imaging where most processing aims to produce a ‘picture’ of the surface as opposed to reconstructing a quantitative model of P - or S -wave velocities.

Fig. 2 illustrates estimated depth to the 410 while Figs 3 and 4 display a series of figures quantifying the relative amplitudes of the measured amplitude of P to S conversion signal generated by the 410. These maps were produced by an amplitude attribute analysis method we developed for this paper. All measurements are made in a fixed depth window. We experimented with a range of scales for the depth interval ranging from 25 to 75 km. All maps like Figs 2–4 in this paper use a depth range of 385–435 km (50 km width). A novel feature of the plane wave migration method implemented by Pavlis (2011b) is that it is a full three-component method. For the EARS data, however, the vertical component is zeroed so only radial and transverse images (Fig. 3) are relevant. Because we have a vector image we also compute sample-by-sample three-component amplitude at each point in the image volume using the L2 norm of each 3-D-vector sample of the image. We will henceforth refer to this as 3C amplitude. For each component (radial, transverse, and 3C amplitude) we compute the following amplitude metrics on a

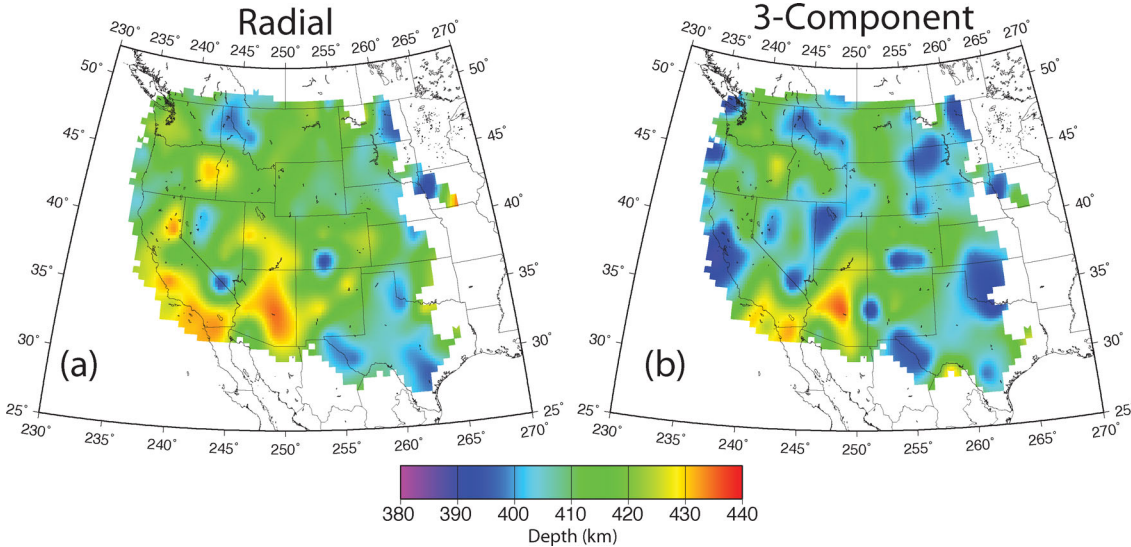


Figure 2. Topography of the 410 estimated from USAArray data and plane wave migration. Both figure display depth to the top of a peak amplitude with the colour scale shown at the bottom of the figures. Depths are inferred from migrated P to S conversion data using AK135 and no crustal corrections using a 50 km depth window and a 100 km radius smoother. Panel (a) is depth inferred from peak amplitude on the radial component image while (b) shows the peak inferred from total amplitude on all three-components.

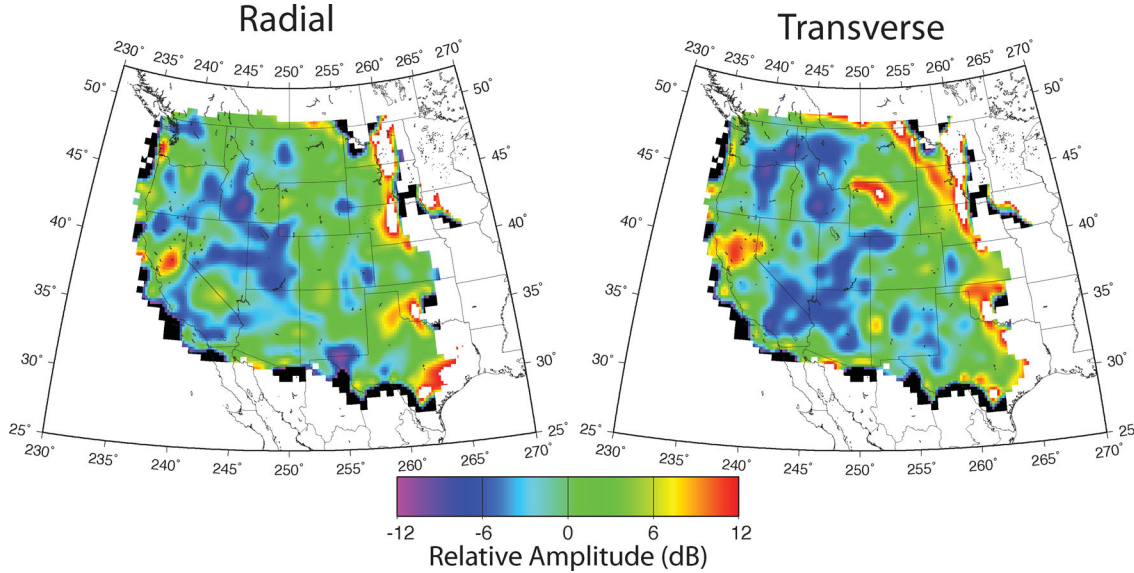


Figure 3. Radial and transverse relative amplitude maps of P to S conversions from the 410. Maps were produced by using the mad amplitude metric applied over a 50 km depth range centered at a depth of 410 km and using GMT's (Wessel & Smith 1995) blockmedian procedure with a 100 km radius. Amplitudes are relative to the median computed from all point measurements made on each component. In all cases null parts of the original image with no data coverage have been excluded from the analysis. Colours are scaled by amplitude in dB with the colour map shown at the bottom of the figure.

uniform mesh of points centered at a depth of 410 km and spanning the entire image volume: (1) rms

$$A_{\text{rms}} = \sqrt{\sum_{i=1}^{N_z} d_{ik}^2}, \quad (7)$$

(2) median absolute distance (mad)

$$A_{\text{mad}} = \text{median}\{|d_{ik}|, i = 1, 2, \dots, N_z\}, \quad (8)$$

and (3) the maximum amplitude of all $|d_{ik}|$. In all cases N_z is the number of samples in the vertical range being analysed (50 points at 1 km intervals in all cases given here) and k is component number (1, 2 or 3 for radial, transverse, or three-component measures). We

use the depth computed at the maximum as a measure of the depth. In practical terms, the maximum amplitude will have the highest variance while the mad will have the least variance (it is commonly used as a robust measure of spread). The rms estimate is between these extremes. This can be seen in Fig. 4, which compares these three measures for three-component amplitudes.

Point measurements of all of these attributes have significant variance, particularly the depth and amplitude estimated from peak values. For this reason the maps in these figures are smoothed with the blockmedian procedure in GMT (Wessel & Smith 1995). This is a reasonable dimension because the Gaussian width parameter is approximately this width at the depth of the 410 with the Fresnel zone width method Pavlis (2011b) used to create this image. The

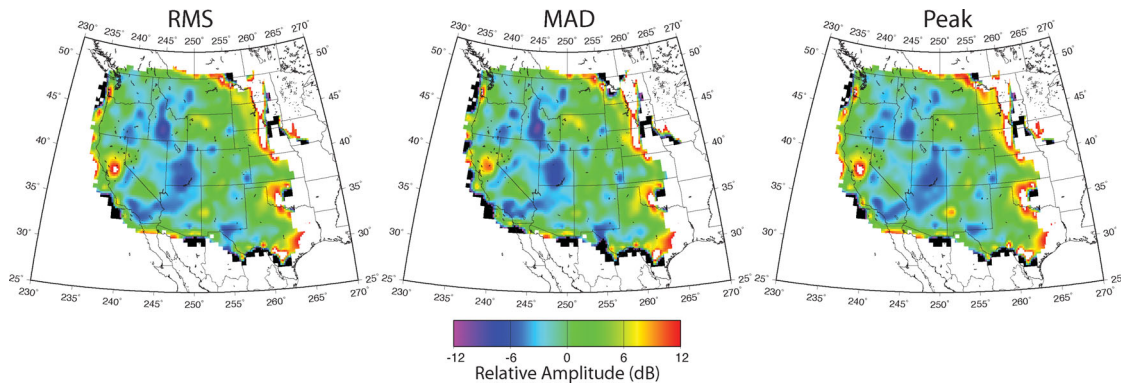


Figure 4. Comparison of different metrics used to compute amplitudes of P to S conversion from the 410. Details of the maps are as described in the caption to Fig. 3 and the colour scale is identical. Here the amplitudes are all computed from the 3C data.

utility of this is demonstrated in Fig. 4 where we see a comparison of all three metrics applied to the 3C amplitudes. That figure demonstrates patterns that are stable and independent of the metric used. On the other hand, comparison with Fig. 3 shows the 3C maps

are very different than that computed from the radial and transverse components. This is an important new observation. One of the objectives of our error analysis is to understand how much of this is believable. An important, final observational result shown in Fig. 5

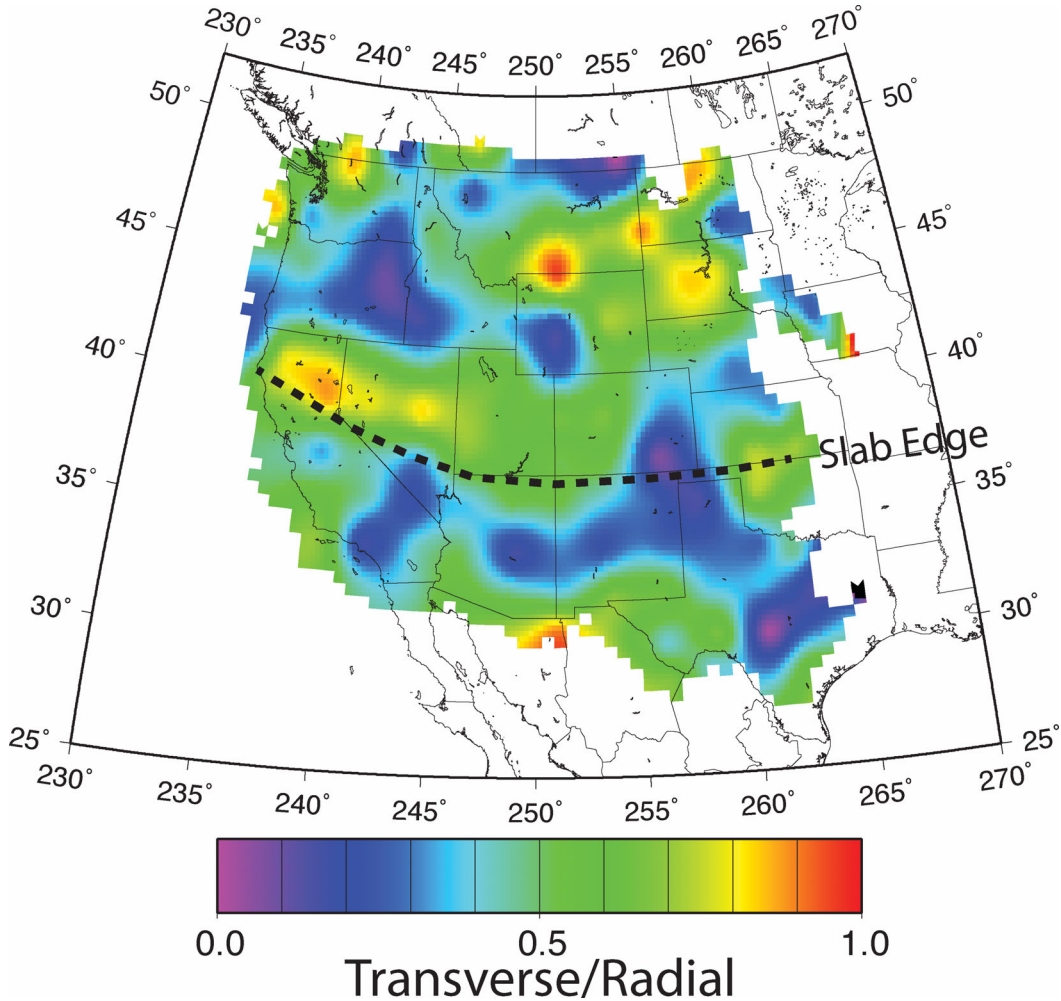


Figure 5. Transverse to radial amplitude ratio of the 410. This map was computed from the maximum amplitude metric (standard 385–435 km depth window) for the transverse component divided by the maximum amplitude on radial component. We chose to use a 200 km radius blockmedian smoother for this figure due to the greater variance that is inevitable in dividing one measured quantity by another. The dashed lines show the map projection of the 3-D, kinematic model of the Farallon slab introduced by Pavlis *et al.* (2012). This prediction differs only slightly from the original model for this geometry of Dickinson & Snyder (1979). Pavlis *et al.* (2012) show that body wave tomography models all show a fast wave speed north of the dashed line and slower speeds at the same depth south of this line consistent with the kinematic model they describe. The high transverse to radial ratio north of the slab edge tracks this trajectory closely to southern Colorado. We note that the model predicts that the top of the Farallon slab has passed through the 410 at approximately the same location.

helps clarify the discrepancy between the radial, transverse, and 3C amplitude maps. This figure shows that the recovered amplitude on the transverse component is, in many areas, nearly as large as the radial component amplitude. As we will show quantitatively in a moment, this observation is completely inconsistent with a single interface with smooth topography.

4 RESOLUTION ANALYSIS

4.1 Migration impulse response

The concept of the migration impulse response (Schneider 1978) is a standard method of appraising the resolution of seismic reflection images. The equivalent for teleseismic P to S imaging, however, has not been defined. One reason is that the irregularities of passive source data make this a more difficult property to characterize or even compute. One of the original motivations for developing the point source, Born approximation modelling method was, in fact, to address this issue. We would argue that the proper measure of migration impulse response for P to S conversion data is to use the point source modelling method for a widely spaced array of point sources and illustrated in Fig. 6. We emphasize that the image illustrated there was produced by a simulation that exactly replicates the (irregular) real recording geometry. This analysis demonstrates three features of the resolving power of this method at the 410. First, the vertical resolution is controlled exclusively by the bandwidth of the signal used in the imaging. Here this simulates the real EARS data where the Gaussian pulse has a width of approximately 1 s, which translates to a depth scale of approximately 10 km. Second, the horizontal scale is controlled by the spatial Gaussian filter used in the pseudo-station, plane wave stacking method Pavlis (2011b). For these data that scale is of the order of 150 km. Finally, the resolution functions are not uniform as illustrated by variations in the detailed geometry of the isosurfaces seen in Fig. 6. This is in contrast to seismic reflection impulse response functions that tend to be nearly constant at a given depth (Yilmaz & Doherty 1987).

4.2 Lateral resolution test

The checkerboard test has become a standard method for appraising resolution in seismic tomography methods. In that context a checkerboard test constructs a velocity model with boxes of a specified size and velocities inside these boxes are set to alternating plus and minus perturbations. The checkerboard model is then used to construct synthetic data matching the data set being analysed and these data are then run through the same inversion procedure as the real data. Fig. 7 illustrates our equivalent for appraising our results at the 410. It provides a complementary single-picture image to the point source image illustrated in Fig. 6. We make three inferences from Fig. 7. First, it clarifies the overall irregularity in resolving power noted above in a single figure. Second, it correctly illustrates that the results are unreliable near the edges of the coverage and, as expected, completely insensitive to areas outside that coverage. Finally, a more subtle result is that the overall total, recovered amplitude is not constant. There is a dim spot under Utah and Arizona which we suspect is a coverage artifact. In any case, it suggests that the observed low amplitude in this region seen in Fig. 4 should be viewed with skepticism.

5 MODELLING RESULTS

5.1 Flat layer model

Fig. 8 shows results comparable to Figs 3 and 5 for the constant amplitude, flat layer model. Liu (2011) validated that the point scattering model using a dense grid of points located at 410 km depth yields a nearly identical solution. The main difference is an inconsistency between the asymptotic approximation used by Beylkin & Burridge (1990) and the approximation used in this simulation. Appendix expands on Liu (2011) to show that unlike the simple convolution of a wavelet with an impulse response used to generate Fig. 8, the Born approximation simulation of the same geometry modifies the wavelet by two terms: (1) convolution with the second time derivative operator as defined in eq. (6) and (2) integration of the point source response over the area of the surface. As shown in

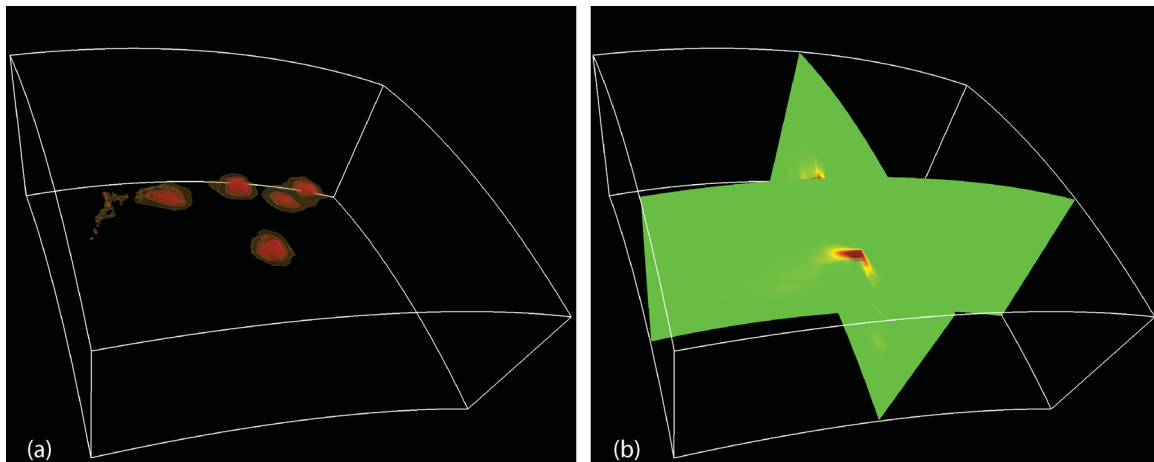


Figure 6. Image of widely spaced point scatters using Gaussian pulse. Contour surfaces are computed for scattering potential equal to 0.73 (red), 0.62 (orange) and 0.48 (yellow), respectively. (a) Contour representation of five point scatters, three of which are at 410 km depth and the other two are at 660 km. Panel (b) shows the same result as (a) using two parallel slices to illustrate more details of how well we recover the point source geometry. The two vertical slices intersect at the nearest point scatter position at 410 km depth. The colour scale of the slices is the same as the coloured isosurfaces in (a).

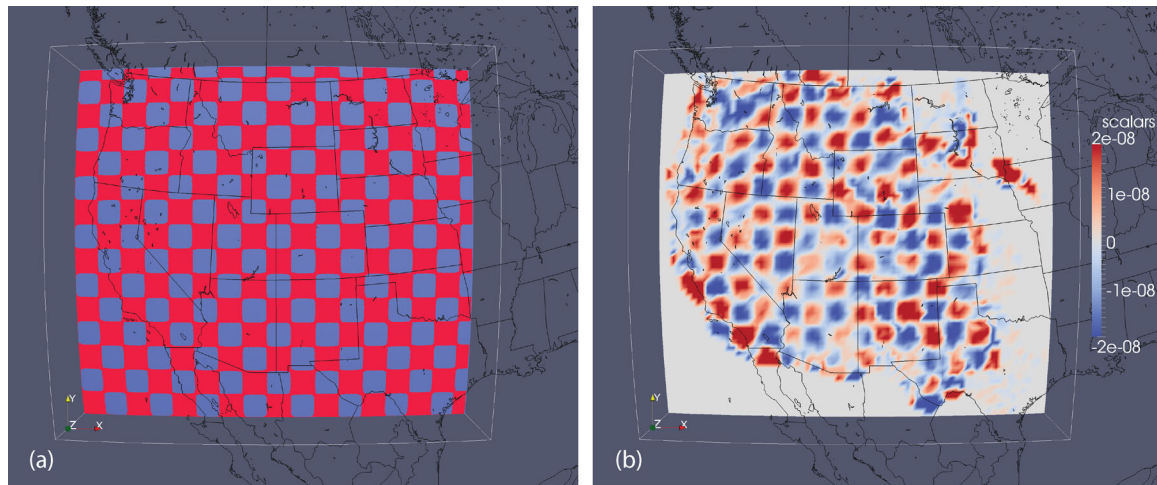


Figure 7. Checkerboard resolution test. Both parts are a 3-D view of slice made at 410 km depth viewed from directly above the center of the image volume. Panel (a) illustrates the original, alternating sign perturbation (checkerboard) model and panel (b) shows the amplitude estimated with the plane wave migration method. Geographic perspective is provided by coastline and state boundary date drawn at a depth of 410 km. The bounding box for the entire image is a spherical shell seen as the white lines around the boundaries of the image. The size of each cell is approximately 156 km.

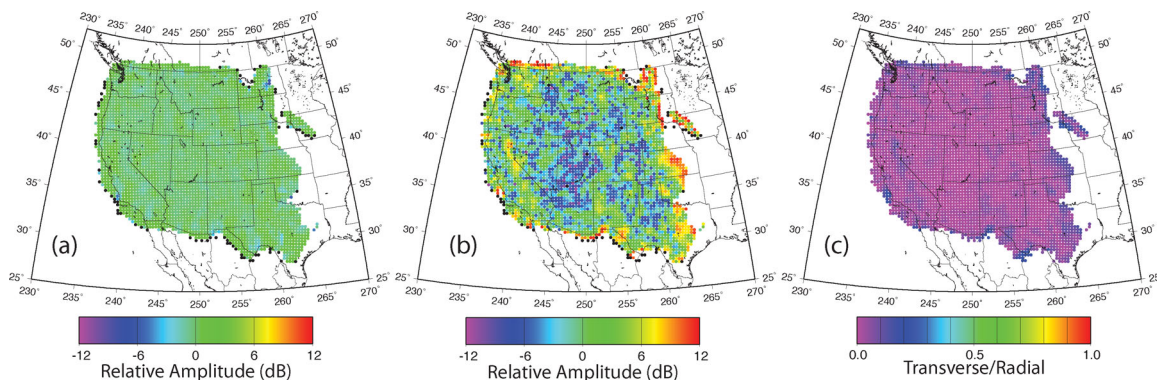


Figure 8. Flat layer simulation amplitude measurements. All components are amplitudes estimated by plane wave migration using the flat layer method to simulate the USArray data geometry. Panel (a) shows relative amplitudes for the radial and panel (b) shows relative amplitudes for the transverse component of the image volume. These are directly comparable to Fig. 3 and use the same colour scaling. Panel (c) shows the amplitude ratio between estimated transverse and radial components and is directly comparable to Fig. 5 including the same colour scale. For this example we did not apply a smoother and display the raw amplitudes at each grid point in the original image volume with a symbol coloured by the scale shown in the legend for each part of the figure.

the appendix the latter yields an operator somewhat like the Hilbert transform whose net effect is to approximately integrate the wavelet in the vertical direction. The net result is that the effective output of a layer simulation with the Born and ray asymptotic approximations in the Beylkin & Burridge (1990) formulation is approximately the time derivative of the incident wavefield. This theoretical detail is important if this approach is used to match waveforms, but has no impact on the relative amplitude maps that are the focus of this paper. That is, relative amplitudes recovered from a Born simulation are virtually indistinguishable from the constant amplitude, flat layer model.

Fig. 8 is an important result for appraisal of 410 amplitude maps seen in Figs 3–5. These figures show that if the 410 were perfectly flat and had a uniform P to S conversion amplitude in the form predicted by standard isotropic layer theory (e.g. Stein & Wysession 2003, pp. 75–86), the recovered amplitude on the transverse component in the data would be tiny compared to the radial component (Fig. 8). The median ratio for this model is 0.044 with lower and upper quartiles of 0.0031 and 0.1083, respectively. The actual data have many points where the ratio approaches unity. Furthermore,

the recovered radial component amplitude (Fig. 8 a) is nearly constant for this simple model. The lower and upper quantiles for the radial amplitude are -0.4 and 0.6 dB respectively, which is a factor of 1/20. This is an enormous contrast to Figs 3 and 4 where the comparable ranges are more than a factor of 10. This indicates the total scattering power of the 410 discontinuity in the western US varies by an order of magnitude since this result shows our migration method accurately recovers relative amplitudes away from the edges of the image volume.

The only caution revealed by this simulation is in the transverse component relative amplitudes illustrated in Fig. 8(b). We see that the relative amplitudes on transverse vary as much as that of the data (Fig. 3). On the other hand, the actual amplitude of the transverse component is generally tiny compared to the radial (Fig. 8c). Related simulations in early validation of this code described in Pavlis (2011b) can explain this observation. He applied this imaging method to data simulated with a 3-D elastic modelling program with a uniform grid of ‘stations’ defined by a decimation of the finite difference grids. In that situation, away from edges transverse component amplitudes were many orders of magni-

smaller than radial. Hence, we conclude Fig. 8 is another representation of the impact of irregular coverage in these data and the transverse relative amplitudes need to be treated with more caution.

5.2 Modelling topography

Fig. 9 shows results from simulation of topography on the 410 at a scale near the lateral resolution limits of the plane wave migration result. The model geometry can be seen in the recovered topography of the surface shown in Fig. 9(a). The model is defined by a single surface centred at a depth of 410 km with an amplitude of 12.5 km (25 km range) and a wavelength of 3° in longitude. Note this means the actual model has a variable wavelength of approximately 312 km at 41°N (307 km at both 51°N and 31°N). Half of this wavelength (156 km) is a useful scale to study the impact of 410 topography on the data because as Fig. 6 shows this is near the nominal lateral resolution scale of these data.

This simulation shows several things that help us understand the real data. First, it gives us confidence that if the 410 were a single surface we can expect to reasonably resolve topography at the

100 km length scale. Secondly, the presence of topography alone can partly explain the large amplitude variations seen in the real data. The scale of relative amplitude fluctuations in this simulation is approximately 1/3 that of the real data. Furthermore, the amplitude fluctuations correlate poorly with the topography in the model but seem more closely linked to variations in the resolution limits seen in Fig. 7. That is, the areas that look most smeared in that figure seem to show the lowest amplitudes on both components. We suggest this can be explained as a smoothing artefact. That is, when the surface can be resolved we recover amplitudes correctly, but when variations are near the lateral resolution of the data like this, variations in data coverage create irregularities in the point resolution functions that distort local amplitudes.

Although topography alone seems capable of producing the observed amplitude fluctuations, Fig. 9(d) shows this model is not able to explain the large transverse to radial amplitude observed in the real data. Furthermore, as Fig. 9 shows the single surface is resolved to a significantly smaller depth range than what is seen in the real data. For that reason, the final simulation we show in the next section combines both a topographic effect and variable amplitudes in what we will call an irregular surface model.

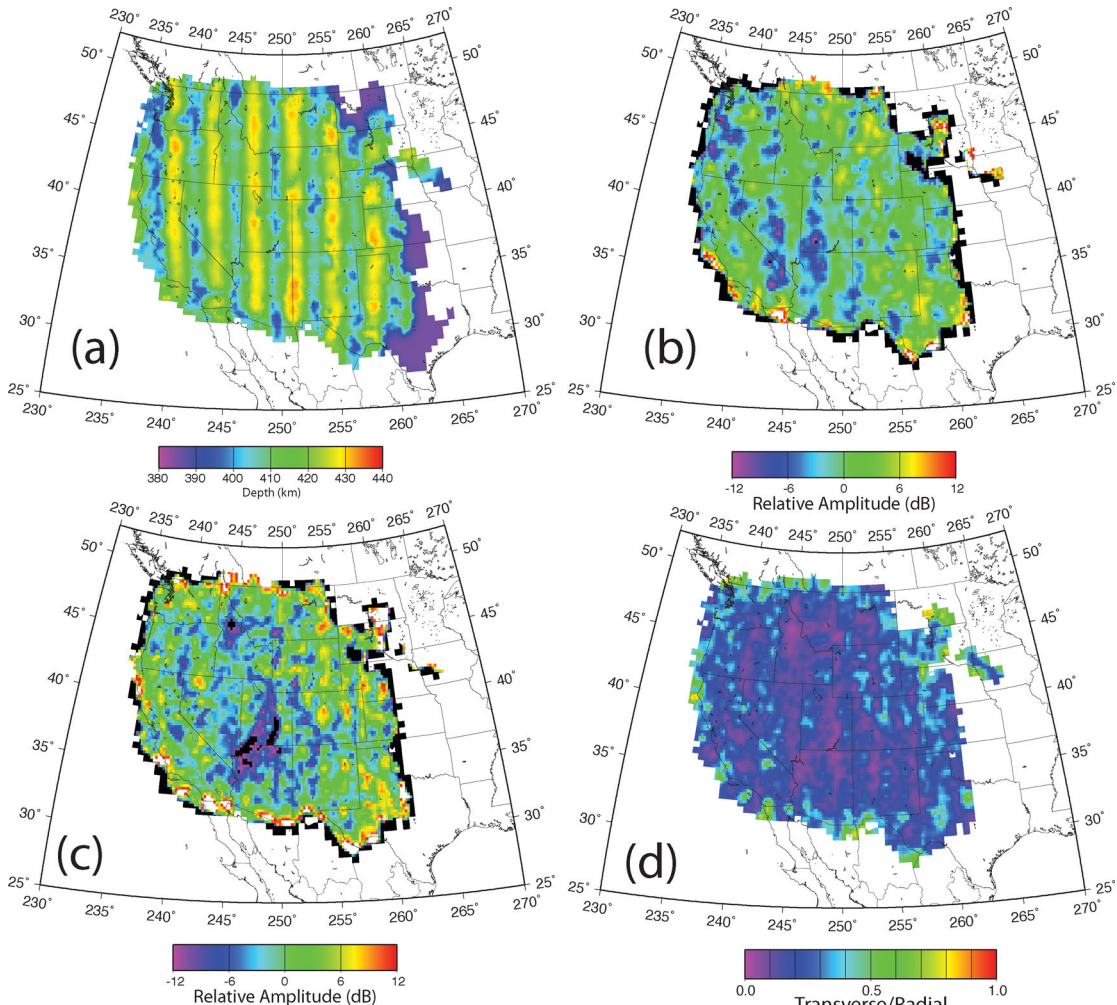


Figure 9. Simulation results for 410 topography simulation. These results were generated from model with a sinusoidal variation of the depth to the 410 with a wavelength of 3° and an amplitude of 12.5 km (25 km range). All figures are maps at a depth of 410 km of attributes computed as described in the text. Panel (a) is recovered depth to the sinusoidal topography model used to generate this simulation. Panels (b) and (c) are estimated relative amplitudes on radial and transverse components, respectively. Colour scale is the same as Fig. 3. These results all used a median smoother with radius of 20 km.

5.3 Rough surface model

Fig. 10 illustrates a model of the 410 that has both topography and amplitude variations smaller than the resolving power of these data with the plane wave method. It was constructed to evaluate a hypothesis made earlier by Pavlis (2011a) that these results suggest that the 410 is an irregular boundary. The model was constructed from the unsmoothed 3C MAD amplitude (Fig. 4 b) and depths (Fig. 2) estimates computed from the data. We constructed a grid with a nominal spacing of 5 km that defines an array of point sources. At each grid point we set the depth of that source as the depth where the 3C MAD metric is maximum and we set the shear modulus perturbation equal to the 3C MAD amplitude estimated from the data at that point. Both the depth and the shear modulus perturbation use the same 50 km depth window we used for the real data. As for the previous simulations the synthetic data were passed through the same processing sequence as the real data and displayed on a map in the same projection. Fig. 11 shows the results.

Fig. 11(a) is directly comparable with Fig. 4(b) because the latter is the Fig. 10 smoothed by the same operator as Fig. 11(a). The results is encouraging as the main features of the amplitude map

is recovered. That is, we properly recover the north–south oriented, low amplitude swath running from Arizona to Idaho and we recover the high amplitude spot under northern California. On the flip side, the results on inferred depth in this model are terrible. Figs 11(c) and 2 should be directly comparable, but they have vague similarities at best. On the other hand, this should not be totally surprising. By design this model has wild variations on short distance scales (Fig. 10 a) that produce synthetic seismograms with rapid lateral variations in waveforms. The imaging cannot perfectly focus this variation because the length scale is shorter than the lateral resolution of the technique, but because the migration operator amounts to a weighted stack (Pavlis 2011b) it cannot remove unfocused energy either. Amplitudes appear to be preserved in this way because we are smoothing all the results at a scale comparable to resolution of the migration. Peak measures, on the other hand, are intrinsically unstable and far more subject of being shifted large distances in the presence of multiple, interfering wave components. Irregular amplitudes and positions used to define this model make every simulated seismogram a superposition of a large number of interfering signals, so it is not surprising that the peak amplitude measurement is unstable in this situation.

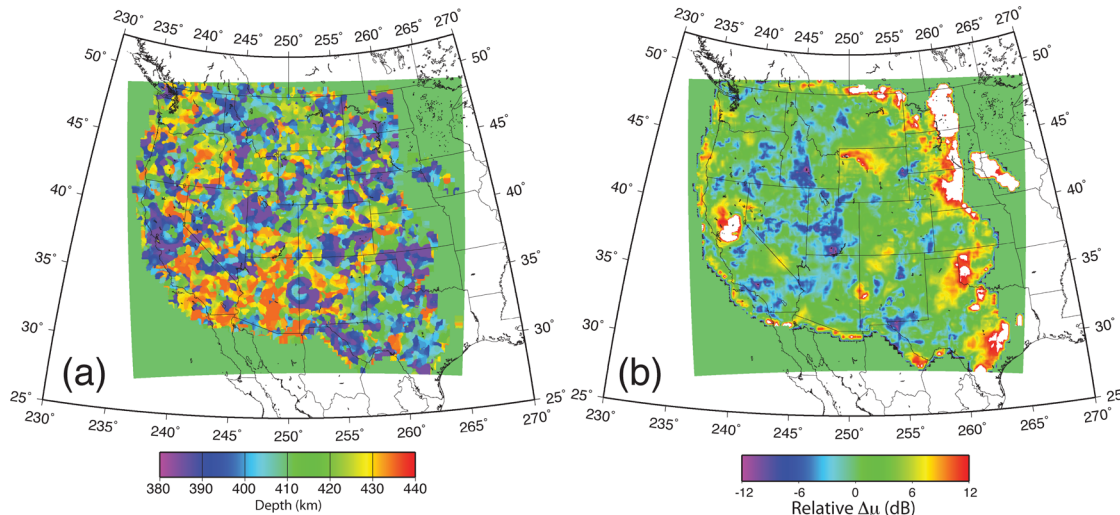


Figure 10. Rough interface model of 410-km discontinuity. Panel (a) shows depth and panel (b) shows relative perturbation of shear modulus of point sources used for this simulation. Point source spacing is nominally 5 km. We scale the perturbation (b) relative to the median and display the result in dB to make the results comparable to the amplitude plots in previous figures. Fig. 4(b) is a function mapped in (b) with a 100 km radius, median smoother applied.

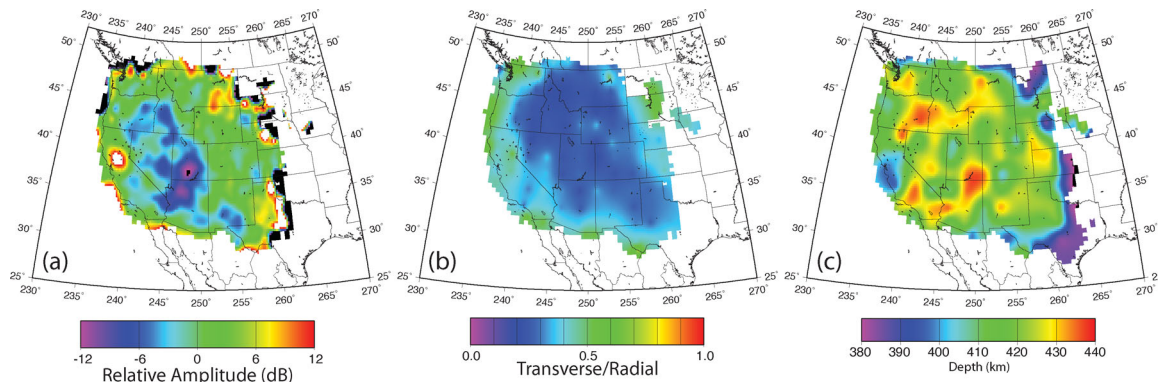


Figure 11. Plane wave imaging results computed from rough model simulation data. All parts of this figure are based on the 3C MAD metric applied on a 50 km depth window and smoothed with a 100 km radius block median operator. Panel (a) shows the recovered amplitude. This should be compared with the true amplitude map with the same smoother illustrated in Fig. 4(b). (b) displays the transverse to radial ratio. Panel (c) illustrates the estimated depth from this simulation. This is comparable to Fig. 2(b) which is the same data as 10(a) smoothed by the same operator as all components of this figure.

6 DISCUSSION

We would assert that this paper has two, complementary elements: (1) introduction of some new ideas for appraising the reliability of scattered wave imaging and (2) some new observations on the nature of the 410. The first is unequivocal and is unlikely to be controversial while the second could prove quite the opposite. For the error appraisal element of this paper we advocate a general approach that all future papers that apply any direct wavefield imaging method could consider. The core idea is to produce simulation data that duplicate the exact geometry of the data being appraised and run that simulation data through exactly the same processing sequence as the real data. The simulation required for this approach must always have four elements: (1) the source and receiver geometry; (2) an Earth model of required seismic properties; (3) a scattering model describing how the scattered wavefield is generated from an incident wavefield and (4) a propagation model describing wave propagation from every point in the medium to each source and receiver. Pavlis (2011a) used this general approach without discussing the more general concepts we advocate here. He used a flat layer, primaries-only, P to S scattering model with ray theory propagators. We extend that approach here to a more flexible approach with a different set of approximations. We again use a radially symmetric earth model and ray propagators but used the point source, single scattering (Born) approximation model of Belykin & Burridge (1990) to model teleseismic P to S conversions. We show how this basic building block can be used to produce point source migration impulse response estimates, a scattered wave imaging equivalent of a checkboard test, and an irregular surface with topography of various scales. All but the first require integration of point response functions over a specified surface, which we implemented by a simple superposition of a large number of point response functions. The integration process revealed a theoretical anomaly discussed in Appendix that needs to be recognized if others elect to apply this approach.

The second element of this paper is the following new observations on the nature of the 410.

(i) This is the first study to consider the relative amplitude of P to S conversions from the 410 beneath the USArray. We find the amplitude of the P to S conversion from the 410 under the western U.S. varies by at least 18 dB. Flat layer simulation shows that if the boundary were perfectly flat with a uniform conversion coefficient the plane wave migration method we applied recovers the resulting boundary with an amplitude variation of less than 1 dB, which is tiny compared to the actual data. The observed amplitude variations show an interesting correlation with inferences made by Pavlis (2011a) and Pavlis *et al.* (2012) about the geometry of the Farallon slab. That is, the amplitude of 410 conversions is lowest between the 300 and 400 km contours Pavlis (2011a) constructed for the top of the Farallon plate. The amplitudes are lowest where the model predicts the material that was once Farallon plate lithosphere is actively passing through the 410.

(ii) No one has previously considered if there is a significant signal observed on the transverse component of P to S conversion data from the 410 recorded on the USArray. We, in fact, find a large signal recorded on the transverse component. For a large fraction of the western United States the transverse/radial amplitude ratio is more than 0.5 with anomalies in the vicinity of Yellowstone and northern California having ratios close to 1.0. We note this directly conflicts with the standard, simple model of the 410 found in freshmen geology textbooks defined by a flat interface separating

two isotropic media. We also find that none of our simulations come close to simulating the observed transverse/radial amplitudes. We note, however, that the only simulation that shows a significant variation at all in the transverse/radial ratio was the long wavelength topography simulation shown in Fig. 9 where ratios as high as 0.3 were common. Other simulations consistently produce maps with this ratio everywhere less than 0.1. This suggests topography at some scale may be a factor in creating the large transverse/radial amplitudes seen in the real data. This observation is a key piece of evidence in favour of the rough 410 km interface model we are proposing here. It is not unambiguous, however, as there are two alternative hypotheses for explaining this observation we cannot currently model: (1) an anisotropic but smooth 410 km interface, or (2) S wave propagators that include the effects of S -wave splitting known to be present throughout the western U.S. (e.g. Long *et al.* 2009).

(iii) Following common practice (e.g. Cao & Levander 2010), we estimated the depth to the 410 from smoothed peak amplitude measurements. The estimates we obtained in this way from the radial component data are roughly comparable to those obtained previously with a completely different algorithm by Cao & Levander (2010). The inferred depth from the radial component (Fig. 2) is shallow under northern Nevada and the Idaho panhandle but depressed under Arizona. We note, however, that Fig. 2(b) produced a significantly different result from the total amplitude on all three components. This is undoubtedly a secondary result of the large transverse amplitude we estimate from these data. The 3C topography estimate has strong similarities to the 3C relative amplitude maps seen in Fig. 4. That is, areas of low amplitude correlate strongly with areas of elevated topography. Given that this low amplitude region is the same area we noted in item 1 which can be linked to the Farallon plate, it supports a model of elevation of the 410 in a region of downwelling created by North America moving over the Farallon plate. Our simulation results confirm that our imaging method is capable of resolving topography of the 410 at 200+ km length scales, but as expected the measurement is less stable than amplitude (Fig. 9).

What do these observations imply about the nature of the 410? We can unambiguously say that beneath the Cordillera of the United States it is definitely not a single, flat interface separating two isotropic media with uniform properties. The flat layer simulations shown here and previously by Pavlis (2011b) make this claim difficult to challenge. Instead, the example image shown in Fig. 12 along with comparable images in Pavlis *et al.* (2012) indicate that the 410 is much more complex and may contain a wealth of unexploited information about the nature of the upper mantle. The amplitude from the conversion is highly variable. It sometimes appears sharp and other times diffuse. Furthermore, it does not seem to generate only P to S conversions in the classic P - SV plane (radial direction), but we record large amplitudes in the transverse direction. Finally, our results suggest the very concept of the ‘topography’ of the 410 as a single surface may be outdated with the resolution made possible by the USArray and our plane wave migration method. Our results, in fact, suggest the 410 is better viewed as a highly irregular scattering zone with roughness on a range of scales. Our results reinforce strongly the following statement made in a recent paper by Tibi & Wiens (2005): ‘This suggests that the 410-km discontinuity may be a more complex feature than previously thought, and current models to explain it are too simplistic.’

If indeed current models are ‘too simplistic’, we suggest most people have a simplistic view for the same reasons we did as

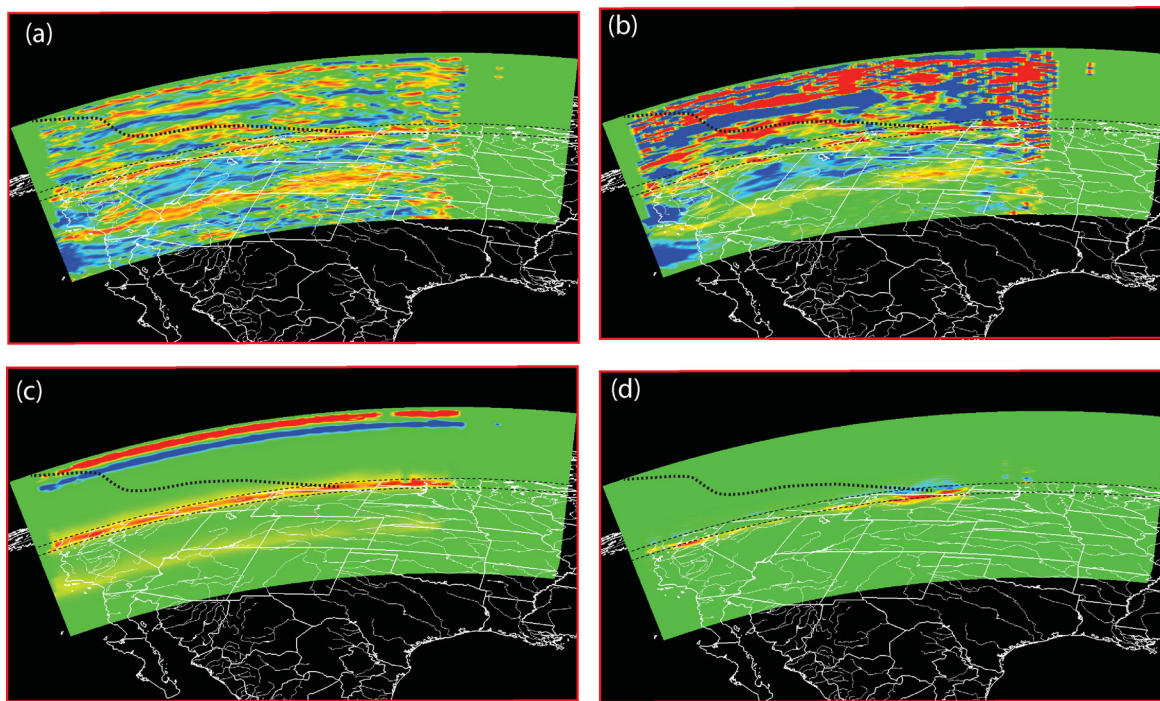


Figure 12. Comparison of section through 3-D migration of real and simulation data sets. All parts of the figure are a common cross-section in true 3-D geometry viewed perpendicular to the line of the section from a view point around central America. The section is approximately the same as section CC' of Pavlis *et al.* (2012) running from near Cape Mendocino in California to northern Minnesota. Geographic data are projected and drawn at a depth of 400 km in white. The dashed lines following the curvature of the earth are a 50-km-wide band centered at 410 km depth. The heavier dashed curve is the model for the top of the Farallon slab described by Pavlis *et al.* (2012). In each section shows amplitude of radial component, P to S conversion, scattering strength. Panels (a) and (b) are identical but (b) is true amplitude while (a) has been processed with an automatic gain control operator. The true amplitude data have a scale of ± 10 with rainbow colour map with positive red and negative blue. The crust and upper mantle section is clipped at this scale to focus on the large amplitude variations that characterize the 410. Panels (c) and (d) are true amplitude sections for two of the simulations described in the text. Panel (c) reconstructed 410 image produced from the flat interface model and (d) is the image produced from the rough surface model. Panels (c) and (d) have the same relative scaling as (b).

newcomers to this subject. That is, we teach students in introductory geology courses that the 410 is the top of the transition zone. We show them standard radially symmetric earth models like PREM and require students to memorize the ‘fact’ that the 410 results from a phase change of olivine. In addition, there is an extensive literature of papers that argue that the 410 has a thickness of less than about 5 km because it scatters short-period P waves (e.g. Benz & Vidale 1993; Vidale *et al.* 1995; Helffrich 2000; Tibi & Wiens 2005). This led us, at least, to have a (likely incorrect) conceptual model of the 410 as a single interface with topography that was a rough thermometer of mantle temperature. However, as pointed out as early as 1993 by Benz and Vidale mineral physics people found observations by seismology that the 410 was sharp hard to accept (see review paper by Helffrich 2000 for a history of this controversy). Furthermore, wide-angle refraction/reflection results on the 410 have consistently argued against a simple interface model. Analysis of data from the Soviet Union’s Deep Seismic Sounding program (ultra long-range refraction experiments using nuclear explosions as sources) showed that the 410 can be modelled as a 15–20-km-thick transition zone (Morozova *et al.* 1999) or an irregular scattering surface (Thybo *et al.* 2003). Melbourne & Helmberger (1988) reached a similar conclusion on the 410 in the southwestern United States through waveform modelling of a rare earthquake in western Texas recorded by stations in California. Thus it seems there have been numerous voices indicating that the simplified model of the 410 as a single interface with topography should be viewed skeptically. Instead this study suggests that the region of the mantle around the 410 may well be a rich mix of unex-

plored phenomena that were previously invisible due to resolution limitation of all previous methods used to probe this feature. For example, there is also no reason to think it is not characterized in places by interleaved sheets of variable properties, particularly in areas of higher strain rate and/or strong vertical motion (see, for example, fig. 2 of Solomatov & Stevenson 1994). We speculate that this could be an explanation for the large transverse/radial amplitude seen in Fig. 5 near Yellowstone and along the predicted edge of the Farallon slab window linked to the creation of the San Andreas fault (Dickinson & Snyder 1979). We suggest this could induce a structural fabric that at these frequencies could behave like an anisotropic media even without lattice preferred orientation.

ACKNOWLEDGEMENTS

The original teleseismic event data for this study came mainly from the Transportable Array component of the USArray facility supported by the National Science Foundation’s Major Research Facility program under cooperative agreement EAR-0350030. This work was supported by the Earthscope Program of the National Science Foundation under EAR-0934289.

REFERENCES

- Aki, K. & Richards, P., 2002. *Quantitative Seismology*, Univ Science Books Sausalito, California, USA.
- Benz, H. & Vidale, J.E., 1993. Sharpness of upper-mantle discontinuities determined from high-frequency reflections, *Nature (London)*, **365**(6442), 147–150.

- Beylkin, G. & Burridge, R., 1990. Linearized inverse scattering problems in acoustics and elasticity, *Wave Motion*, **12**(1), 15–52.
- Bostock, M., 2002. Kirchhoff-approximate inversion of teleseismic wavefields, *Geophys. J. Int.*, **149**(3), 787–795.
- Cao, A. & Levander, A., 2010. High-resolution transition zone structures of the Gorda slab beneath the western United States: implication for deep water subduction, *J. geophys. Res.*, **115**(B07301), doi:10.1029/2009JB006876.
- Crotwell, H.P., 2007. High data volume seismology: surviving the avalanche, *PhD thesis*, University of South Carolina.
- Crotwell, H.P. & Owens, T.J., 2005. Automated receiver function processing, *Seism. Res. Lett.*, **76**(6), 702–709.
- Dickinson, W.R. & Snyder, W.S., 1979. Geometry of triple junctions related to San Andreas transform, *J. geophys. Res.*, **84**(B2), 561–572.
- Dueker, K.G. & Sheehan, A.F., 1997. Mantle discontinuity structure from midpoint stacks of converted P to S waves across the Yellowstone hotspot track, *J. geophys. Res.*, **102**, 8313–8327.
- Dueker, K.G. & Sheehan, A.F., 1998. Mantle discontinuity structure beneath the Colorado Rocky Mountains and high plains, *J. geophys. Res.*, **103**(B4), 7153–7169.
- Eagar, K.C., Fouch, M.J. & James, D.E., 2010. Receiver function imaging of upper mantle complexity beneath the Pacific Northwest, United States, *Earth planet. Sci. Lett.*, **297**, 141–153.
- Efron, B., 1979. Bootstrap methods: another look at the jackknife, *Ann. Stat.*, **7**(1), 1–26.
- Helffrich, G., 2000. Topography of the transition zone seismic discontinuities, *Rev. geophys.*, **38**(1), 141–158.
- Langston, C.A., 1979. Structure under Mount Rainier, Washington, inferred from teleseismic body waves, *J. geophys. Res.*, **84**(B9), 4749–4762.
- Levander, A., Niu, F. & Symes, W., 2005. Imaging teleseismic P to S scattered waves using the Kirchhoff integral, *Geophys. Monogr.-Am. Geophys. Un.*, **157**, 149–169.
- Ligorría, J.P. & Ammon, C.J., 1999. Iterative deconvolution and receiver-function estimation, *Bull. seism. Soc. Am.*, **89**(5), 1395–1400.
- Liu, X., 2011. Appaising the reliability of scattered wavefield imaging, *Master's thesis*, Indiana University.
- Long, M.D., Gao, H., Klaus, A., Wagner, L.S., Fouch, M.J., James, D.E. & Humphreys, E., 2009. Shear wave splitting and the pattern of mantle flow beneath eastern Oregon, *Earth planet. Sci. Lett.*, **288**(3–4), 359–369.
- Melbourne, T. & Helmberger, D., 1988. Fine structure of the 410-km discontinuity, *J. geophys. Res.*, **103**, 10091–10102.
- Morozova, E.A., Morozov, I.B. & Smithson, S.B., 1999. Heterogeneity of the uppermost mantle beneath Russian Eurasia from the ultra-long range profile quartz, *J. geophys. Res.*, **104**(B4), 20329–30348.
- Niu, F., Levander, A., Cooper, C.M., Lee, C.-T.A., Lenardic, A. & James, D.E., 2004. Seismic constraints on the depth and composition of the mantle keel beneath the Kaapvaal craton, *Earth planet. Sci. Lett.*, **224**(3–4), 337–346.
- Nowack, R.L., Dasgupta, S., Schuster, G.T. & Sheng, J.-M., 2006. Correlation migration using Gaussian beams of scattered teleseismic body waves, *Bull. seism. Soc. Am.*, **96**(1), 1–10.
- Pavlis, G.L., 2003. Imaging the earth with passive seismic arrays, *Leading Edge*, **22**(3), 224–231.
- Pavlis, G.L., 2011a. Three-dimensional wavefield imaging of data from the USArray: new constraints on the geometry of the Farallon slab, *Geosphere*, **7**(3), 785–801.
- Pavlis, G.L., 2011b. Three-dimensional, wavefield imaging of broadband seismic array data, *Comput. Geosci.*, **37**(8), 1054–1066.
- Pavlis, G.L., Sigloch, K., Burdick, S., Fouch, M.J. & Vernon, F.L., 2012. Unraveling the geometry of the Farallon plate: synthesis of three-dimensional imaging results from the USArray, *Tectonophysics*, **532–535**, 82–102.
- Poppeliers, C. & Pavlis, G.L., 2003a. Three-dimensional, prestack, plane wave migration of teleseismic P-to-S converted phases: 1. theory, *J. geophys. Res.*, **108**(B2), 2112, doi:10.1029/2001JB000216.
- Poppeliers, C. & Pavlis, G.L., 2003b. Three-dimensional, prestack, plane wave migration of teleseismic P-to-S converted phases: 2. Stacking multiple events, *J. geophys. Res.*, **108**(B5), 2267, doi:10.1029/2001JB001583.
- Ringwood, A., 1975. *Composition and Petrology of the Earth's Mantle*, Vol. **618**, McGraw-Hill, New York.
- Schneider, W., 1978. Integral formulation for migration in two and three dimensions, *Geophysics*, **43**(1), 49–76.
- Shearer, P.M., Flanagan, M.P. & Hedlin, M.A.H., 1999. Experiments in migration processing of SS precursor data to image upper mantle discontinuity structure, *J. geophys. Res.*, **104**(B4), 7229–7242.
- Sheehan, A., Shearer, P., Gilbert, H. & Dueker, K., 2000. Seismic migration processing of P-SV converted phases for mantle discontinuity structure beneath the Snake River plain, Western United States, *J. geophys. Res.*, **105**(B8), 19055–19065.
- Solomatov, V.S. & Stevenson, D.J., 1994. Can sharp seismic discontinuities be caused by non-equilibrium phase transformations?, *Earth planet. Sci. Lett.*, **125**, 267–279.
- Stein, S. & Wysession, M., 2003. *An Introduction to Seismology, Earthquakes, and Earth Structure*, Wiley-Blackwell, Malden, MA, USA.
- Thybo, H., Nielsen, L. & Perchue, E., 2003. Seismic scattering at the top of the mantle transition zone, *Earth planet. Sci. Lett.*, **216**, 259–269.
- Tibi, R. & Wiens, D.A., 2005. Detailed structure and sharpness of upper mantle discontinuities in the Tonga subduction zone from regional broadband arrays, *J. geophys. Res.*, **110**(B06313), doi:10.1029/2004JB003433.
- Vidale, J.E., Ding, X.Y. & Grand, S.P., 1995. Upper-mantle discontinuities: a sharpness estimate from near-critical reflections, *Geophys. Res. Lett.*, **22**, 2557–2560.
- Vinnik, L., 1977. Detection of waves converted from P to SV in the mantle, *Phys. Earth planet. Inter.*, **15**(1), 39–45.
- Weglein, A.B. et al., 2003. Inverse scattering series and seismic exploration, *Inverse Problems*, **19**(6), R27–R83.
- Wessel, P. & Smith, W., 1995. The generic mapping tools (GMT) software.
- Wilson, C.K., Shragge, J. & Artman, B., 2004. *Teleseismic imaging with wave equation migration*, vol. **85**, pp. @abstract S33A–1091, American Geophysical Union, Washington, DC, United States (USA), United States (USA).
- Wu, R. & Aki, K., 1985a. Scattering characteristics of elastic waves by an elastic heterogeneity, *Geophysics*, **50**, 582–595.
- Wu, R.S. & Aki, K., 1985b. Elastic wave scattering by a random medium and the small-scale inhomogeneities in the lithosphere, *J. geophys. Res.*, **90**(B12), 10261–10273.
- Yilmaz, O. & Doherty, S., 1987. *Seismic data processing*, vol. 2, Society of Exploration Geophysicists, Tulsa, OK.

APPENDIX A: INTEGRATION OF POINT SCATTERERS TO APPROXIMATION TO A DISCONTINUITY SURFACE

This section addresses a theoretical disconnect between the point source theory and the more standard theory of reflection/transmission coefficients based on a singularity in the velocity and/or density of the medium. The singularity theory predicts a delta function scattering response, which for the problem addressed in this paper is commonly called the P to S transmission coefficient. Yet, the perturbation theory integral formulation in eq. (6) requires the source wavelet to be modified by a second derivative in time operator. Here we show this apparent inconsistency is resolved in the volume integration. That is, we show that integration of the point source formula for plane wave illumination over a flat surface with a finite thickness produces a form comparable to the delta function response predicted by the standard plane wave, reflection/transmission theory.

Eq. (6) gives the form of the vector displacement of P-to-S converted wave that is the core component of our point source simulation method. For this analysis we consider only the scalar value of the converted wave displacement and neglect the scattering pattern $f^{PS}(\theta^{PS})$. Eq. (6) then reduces to

$$\Delta u^{PS}(t) = \int_D \hat{A}b(t) *_t \delta(t - \phi^P - \phi^S) dx dy dz, \quad (A1)$$

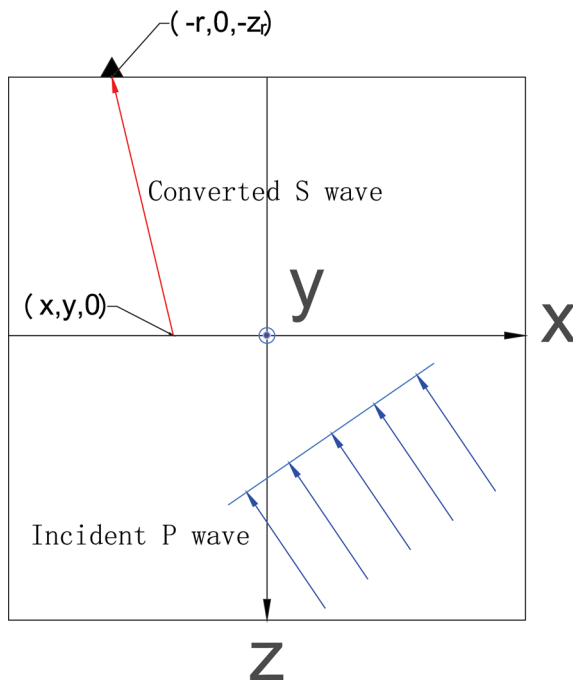


Figure A1. The response of a very thin horizontal discontinuity layer, the thickness of which is Δz . An integral over the entire discontinuity layer gives the P -to- S phases on a single station. The discontinuity layer is at $z = 0$.

where $\hat{A} = \frac{1}{\phi^S}$ is the geometric spreading amplitude. For this analysis we assume the source wavelet is a Gaussian wavelet. In that case $b(t)$ is the 2nd derivative of a Gaussian function which has the property

$$\int_{-\frac{T}{2}}^{\frac{T}{2}} b(t) dt = 0. \quad (\text{A2})$$

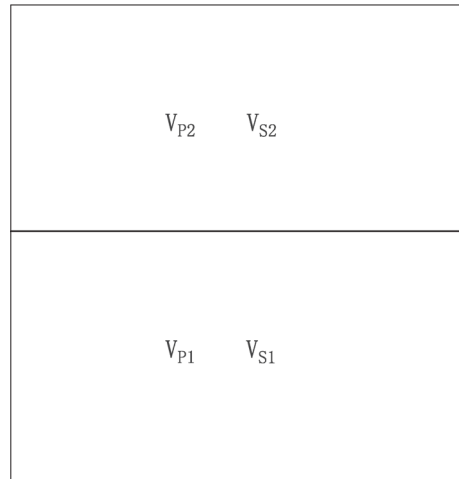


Figure A2. The P -to- S scattering response of an interface between two layers. An integral over the upper layer gives the P -to- S phases on a single station. The depth of the interface is at $z = 0$. The superposition of thin discontinuity layer responses at depth from $z = -z_r$ to $z = 0$ gives the response of an interface.

Consider the case of a very thin discontinuity layer in the reference media with thickness Δz and uniform perturbation values. In this case eq. (A1) can be reduced to

$$\Delta u^{PS}(t) = \Delta z \int_{\Omega} \frac{1}{\phi^S} b(t) *_{\ell} \delta(t - \phi^P - \phi^S) dx dy. \quad (\text{A3})$$

The total traveltime τ is,

$$\begin{aligned} \tau &= \phi^P + \phi^S \\ &= -px + C_0 + \frac{\sqrt{(x+r)^2 + y^2 + z_r^2}}{V_S}, \end{aligned} \quad (\text{A4})$$

where p is the ray parameter for incident P wave and C_0 is a constant for plane P -wave traveltime at the origin $(0, 0, 0)$.

Apply a change of variables from (x,y) to (τ, θ) and eq. (A4) becomes

$$\Delta u^{PS}(t) = \Delta z \int_{\tau_m}^{\infty} d\tau \int_0^{2\pi} \frac{1}{\tau - \phi^P} b(t - \tau) |J| d\theta, \quad (\text{A5})$$

where θ is the angle when (x,y) is converted to polar coordinates $\theta = \arctan(y/x)$ (see Fig. A1). $\tau_m = \min(\phi^P + \phi^S)$ is the traveltime for earliest arrival of scattered wave (Fermat's principle). J is the Jacobian matrix,

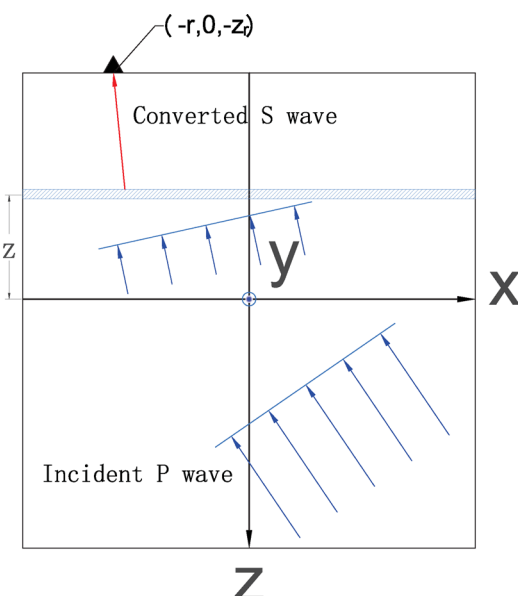
$$|J| = \begin{vmatrix} \frac{\partial x}{\partial \tau} & \frac{\partial x}{\partial \theta} \\ \frac{\partial y}{\partial \tau} & \frac{\partial y}{\partial \theta} \end{vmatrix} = \frac{2V_S^2(\tau - \phi^P)}{\sqrt{1 - V_S^2 p^2}}. \quad (\text{A6})$$

Substituting $|J|$ into eq. (A5) and integrating over θ , we get

$$\Delta u^{PS}(t) = \Delta z \int_{\tau_m}^{\infty} \frac{4\pi V_S^2}{\sqrt{1 - V_S^2 p^2}} b(t - \tau) d\tau. \quad (\text{A7})$$

Eq. (A7) shows that a thin discontinuity layer produces scattered phases comparable to the time integral of the 2nd derivative of Gaussian wavelet $b(t)$, or equivalently the first derivative of a Gaussian wavelet.

Now we generalize eq. (A7) to approximate the scattered wave produced by the interface between two layers. Applying the law of superposition, we divide the upper layer into many infinitely thin



horizontal slices at different depths. For each thin slice, the scattered P -to- S phase can be computed from eq. (A7). We define

$$f(t - \tau_m) = \int_{\tau_m}^{\infty} \frac{4\pi V_{S2}^2}{\sqrt{1 - V_{S2}^2 p^2}} b(t - \tau) d\tau, \quad (\text{A8})$$

where V_{S2} is the shear wave velocity in the upper layer (Fig. A2).

According to Snell's law, the incident P wave and converted S wave ray paths that correspond to the least traveltime τ_m have the same ray parameter. Therefore, τ_m is a linear affine function of the horizontal slice depth z ,

$$\tau_m = \min(\phi^P + \phi^S) = kz + C. \quad (\text{A9})$$

As a result, the scattered wavefield displacement generated by the upper layer is

$$u^{PS}(t) = \int_{-z_r}^0 f(t - \tau_m) dz = \int_{\tau_{m_0}}^{\tau_{m_1}} \frac{1}{k} f(t - \tau_m) d\tau_m, \quad (\text{A10})$$

where k is a constant, $\tau_{m_1} = C$ is the least traveltime for scattered phases generated by the interface between two layers, and we make $\tau_{m_0} = -kz_r + C < -T/2$ and $t > 0$.

From eq. (A2) and the fact that $b(t)$ is the 2nd derivative of a Gaussian function, we derive that $f(t)$ is also DC-balanced,

$$\int_{-\frac{T}{2}}^{\frac{T}{2}} f(t) dt = 0. \quad (\text{A11})$$

Combining eq. (A10) and (A11), we arrive at

$$u^{PS}(t) \neq 0 \text{ if and only if } t \in \left(\tau_{m_1} - \frac{T}{2}, \tau_{m_1} + \frac{T}{2} \right) \quad (\text{A12})$$

and $u^{PS}(t)$ is the double time integral of $b(t)$, the 2nd derivative of a Gaussian function. Therefore, $u^{PS}(t)$ is a good estimation of the P -to- S displacement field produced by an interface analogous to 410 discontinuity.

This derivation indicates that theoretically the integration of point scatters on a subsurface could approximate a thin discontinuity surface, and a similar integral over a volume with a finite thickness is a good approximation to the response of an interface between two layers.